



Photogenerated charge transfer via interfacial internal electric field for significantly improved photocatalysis in direct Z-scheme oxygen-doped carbon nitrogen/CoAl-layered double hydroxide heterojunction



Yan Wu^a, Hou Wang^{a,b,*}, Yuanmiao Sun^c, Tong Xiao^a, Wenguang Tu^a, Xingzhong Yuan^b, Guangming Zeng^b, Shuzhou Li^c, Jia Wei Chew^{a,d,*}

^a School of Chemical and Biomedical Engineering, Nanyang Technological University, Singapore 637459, Singapore

^b College of Environmental Science and Engineering, Hunan University, Changsha 410082, PR China

^c School of Materials Science and Engineering, Nanyang Technological University, Singapore 639798, Singapore

^d Singapore Membrane Technology Center, Nanyang Environment and Water Research Institute, Nanyang Technological University, Singapore 639798, Singapore

ARTICLE INFO

Keywords:

Environmental remediation
Internal electric field
Oxygen-doped carbon nitride
Layered double hydroxide
Heterostructure

ABSTRACT

Semiconductor heterojunctions, widely applied in photocatalytic solar-to-chemical energy conversion, are advantageous for spatially separating photogenerated charge across the heterojunction boundary, inhibiting carrier recombination processes and synergistically accelerating photocatalytic reaction beyond individual components. Herein, a novel type of 2D–2D heterostructure consisting of oxygen-doped carbon nitride (OCN) and ultrathin CoAl-layered double hydroxide (CoAl-LDH) with the aid of hydrogen bonding has been constructed via *in situ* growth method. The visible-light photocatalytic degradation efficiency of the hybridized photocatalyst is 38 and 239 folds higher than that of pure OCN and pure CoAl-LDH, respectively. This is due to the strong electronic coupling effect in the heterostructured interface, which induces photogenerated charge transfer from CoAl-LDH to OCN and make for the constriction of an interfacial internal electric field (IIEF) between CoAl-LDH and OCN. Based on the experimental evidence and density functional theory calculations, an IIEF-induced direct Z-scheme charge transfer mechanism has been proposed to enhance the extraction and utilization of photoinduced electron and hole in respectively CoAl-LDH and OCN. This work uncovers the nature of charge transfer system based on a 2D–2D heterostructured system, which can be potentially employed in various fields of photocatalysis.

1. Introduction

Solar energy harvesting and conversion have evoked much attention in chemical synthesis, energy generation and addressing environmental issues [1–4]. For practical application, favorable photocatalysts are required to achieve excellent solar light absorption and fast conversion [5,6]. Despite a great deal of research from organic materials to inorganic semiconductors, most developed photocatalysts with single components are disadvantageous in terms of complex synthesis, poor light utilization, weak photostability and fast recombination of photo-induced carrier separation [7,8]. In order to solve these problems, the development of elaborate hybrid semiconductors is considered as an effective way [2,9].

Since the discovery of graphene was the subject of the Nobel Prize in Physics in 2010, photocatalyst design on the nanostructured semiconductor has extended to two dimensional (2D) materials including transition metal dichalcogenides, hexagonal boron nitride, graphite

carbon nitride, layered metal hydroxides and metal/covalent organic frameworks [10–13]. Owing to the flexible tunability of metal ions, (relative) ease of scale-up, visible-light-response performance, full surface hydroxyl groups and 2D anisotropy with nanometer thickness, layered double hydroxides (LDHs) with the general expression of $[M_{1-x}^{2+}M_x^{3+}(OH)_2](A^{n-})^{x/n} \cdot mH_2O$ (where M^{2+} and M^{3+} are respectively divalent and trivalent metals, and A^{n-} is a charge-balancing anion) have become promising materials in photocatalysis [14–16]. Zhao et al. reported that the ultrathin ZnAl-layered double hydroxide was a superior photocatalyst for the photoreduction of CO_2 to CO in water under visible light irradiation because of the coordinately unsaturated Zn^{+} centers within the nanosheets [17]. The single-layer CoAl-layered double hydroxides with CO_3^{2-} counterions, prepared by Li et al., had a specific surface area of $\sim 289 \text{ m}^2 \text{ g}^{-1}$ and excellent electrocatalytic oxygen evolution efficiency [18]. The CoAl-layered double hydroxides semiconductor with the band gap of 2.1 eV serving as the visible light absorber was hybridized with P25, and the composites

* Corresponding authors at: School of Chemical and Biomedical Engineering, Nanyang Technological University, Singapore 637459, Singapore.

E-mail addresses: huankewanghou024@163.com (H. Wang), jchew@ntu.edu.sg (J.W. Chew).

exhibited good activity and selectivity (> 90%) for aqueous CO_2 photoreduction to CO [19]. However, pristine LDHs generally exhibit poor crystalline orientation, slow charge carrier mobility and rapid recombination rates of electron-hole pairs, which restrict the quantum efficiency and photocatalytic activity under solar irradiation [20]. Constructing heterogeneous systems like van der Waals heterostructure (i.e., stacks of 2D atomic crystals) provide new possibilities in adjusting the electronic state at the surface of LDH crystals. With the differences in work function and the presence of nanoreactors in space or sandwich structures between different 2D crystals, photochemical reactivity of LDHs can be ultimately controlled [21–23].

Our previous research indicated that the metal-free polymer, graphitic carbon nitride ($\text{g-C}_3\text{N}_4$), exhibit good visible light response, and is promising in photochemical process [12,24,25]. Furthermore, excellent photocatalytic performance of $\text{g-C}_3\text{N}_4$ in environmental remediation can be obtained by heteroatom doping strategy via enhancing light trapping, tuning the band gap structure and creating more active sites [5,26]. Two dimensional (2D) oxygen-doped carbon nitride (OCN) has the C–O or O–C–N bonds on the surface [27–31], which can further bond with $-\text{OH}$ groups on the LDHs surface, and thus more electron-transfer pathways between OCN and LDHs are available. In addition, compared with pure C_3N_4 , the OCN has narrower band gap, improved solar absorption and prolonged the life expectancy for photoexcited carriers [28,32]. It can be expected that the hybridization of OCN with LDHs would provide a feasible way to improve charge carrier transfer and separation. Such a hybridized system has the following advantages: (i) favorable redox potentials due to respective conductor band and valence band, (ii) enabling a strong electronic coupling at the heterojunction interface for highly efficient separation of photoinduced electron-hole pairs, (iii) providing a versatile platform to facilitate the understanding of the interfacial effect between 2D-2D semiconductor structure in the improvement of photocatalytic performance.

In this work, the 2D-2D OCN/CoAl-LDH (OCAL) hybrids with interconnected flower-like structure were prepared by a facile *in situ* hydrothermal method (Fig. 1). The resultant materials showed a significantly improved photocatalytic degradation efficiency towards pollutant removal in water upon visible light illumination, with a degradation rate of 0.09568 min^{-1} , which was 38 and 239 folds than that of pure OCN and pure CoAl-LDH, respectively. The strong electronic coupling in the hybridized heterostructure interface could induce charge transfer from CoAl-LDH to OCN and be beneficial to the formation of interfacial internal electric fields (IIEF) between CoAl-LDH and OCN. A IIEF-induced direct Z-scheme charge transfer mechanism had occurred under visible-light-driven excitation, with the recombination between the electron of OCN and the hole of CoAl-LDH

enhancing the extraction and utilization of photoinduced electron (or hole) in CoAl-LDH (or OCN), which further facilitates the radical generation and photocatalytic degradation performance. The stable OCN/CoAl-LDH photocatalyst can be potentially employed in photocatalysis and photoelectrochemical devices.

2. Experiment

2.1. Materials

Urea, oxalic acid, methanol, cobalt(II) nitrate hexahydrate ($\text{Co}(\text{NO}_3)_2 \cdot 6\text{H}_2\text{O}$), aluminum nitrate nonahydrate ($\text{Al}(\text{NO}_3)_3 \cdot 9\text{H}_2\text{O}$), ethylenediaminetetraacetic acid disodium salt (EDTA-2Na), ammonium fluoride, *p*-benzoquinone and isopropyl alcohol were purchased from Sigma-Aldrich Co., Ltd. All reagents and solvents were of analytical reagent grade and used as received.

2.2. Synthesis of OCN/CoAl-LDH hybrids

The porous oxygen-doped graphic carbon (OCN) samples were prepared by calcining the mixture of oxalic acid and urea under high temperature [32]. Specifically, 20 g of urea was mixed with 8 g of oxalic acid by grinding in a mortar. The mixture was put into a crucible with a cover, and then heated at 550°C in a muffle furnace for 5 h at a heating rate of $10^\circ\text{C min}^{-1}$. The resultant brown powder was collected for further use. The oxygen amount in carbon nitride was 3.6 wt% from the Fig. S1a in Supporting Information. The mesoporous OCN had a surface area of $159.1 \text{ m}^2 \text{ g}^{-1}$ and pore volume of $0.73 \text{ cm}^3 \text{ g}^{-1}$ (Fig. S1b), which provides the beneficial feature for metal ions accumulation. This kind of OCN/CoAl-LDH hybrids were synthesized via a facile procedure. Specifically, a transparent and homogeneous solution was formed by adding 2.6478 g $\text{Co}(\text{NO}_3)_2 \cdot 6\text{H}_2\text{O}$, 0.9378 g $\text{Al}(\text{NO}_3)_3 \cdot 9\text{H}_2\text{O}$, 1.5 g urea and 0.3704 g NH_4F into 35 mL of deionized water under agitation. Then a targeted amount of OCN powder (10 mg, 30 mg, 50 mg and 100 mg) was dispersed into the mixture solution with the aid of ultrasonication. Finally, the dispersion was transferred into a Teflon-lined stainless steel autoclave and hydrothermally treated at 110°C for 24 h. The resulting hybrids were washed with water and ethanol thoroughly, and then dried at 60°C under vacuum. The as-obtained hybrids were denoted as OCAL-1, OCAL-3, OCAL-5 and OCAL-10 (with the numbers signifying the amounts of OCN powder added in mg), in which the OCN mass percentage was 3.6%, 10.8%, 18.0% and 36.0%, respectively. For comparison purposes, pure CoAl-LDH was prepared in the absence of OCN under similar conditions.

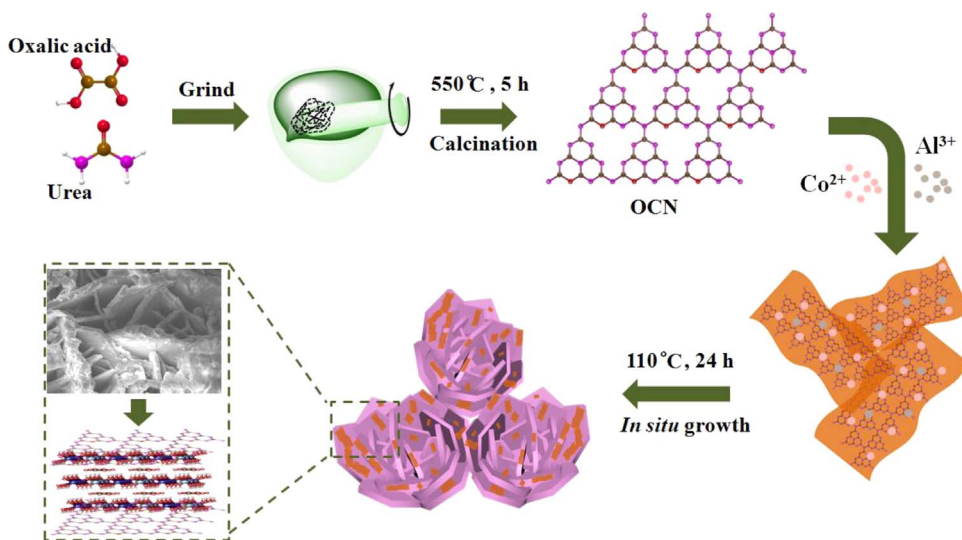


Fig. 1. Schematic of synthesis process for OCN/CoAl-LDH hybrids.

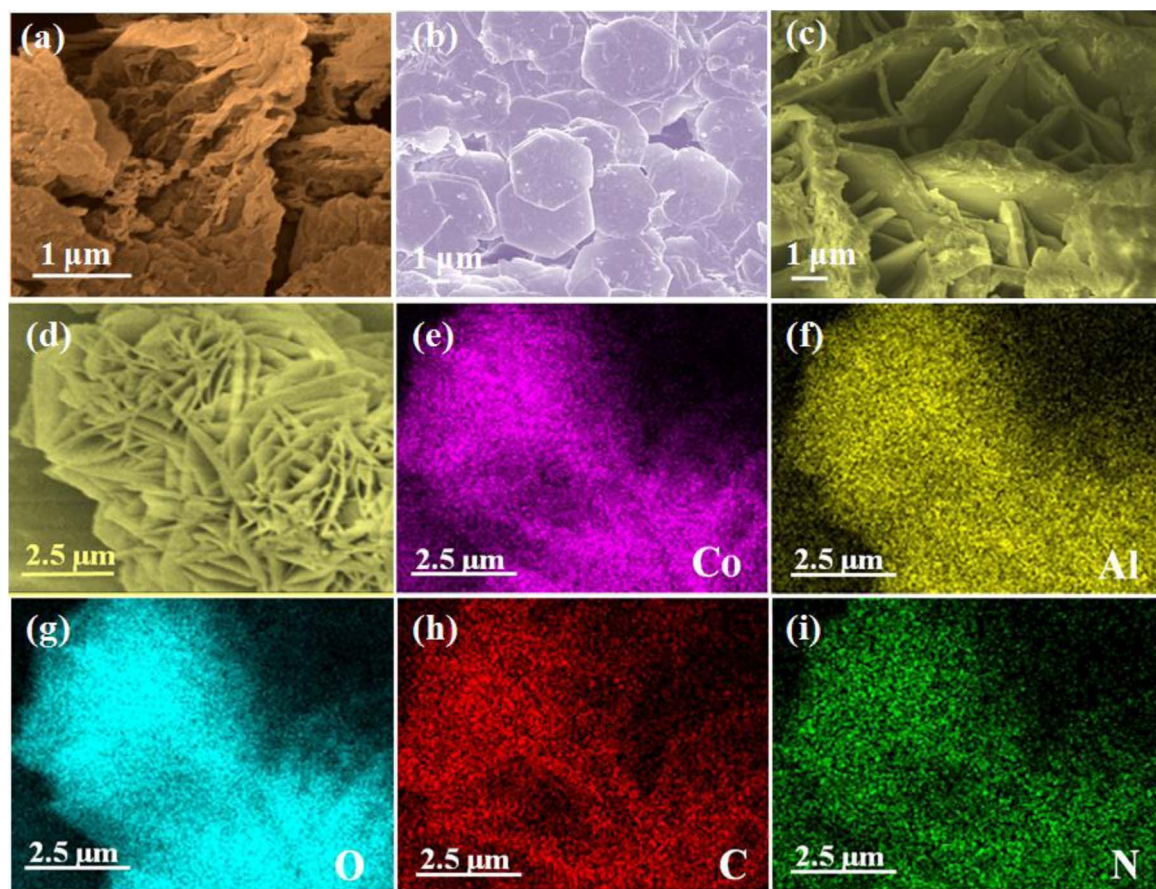


Fig. 2. SEM images of (a) pure OCN, (b) pure CoAl-LDH, and (c) OCAL-5; (d) lower-magnification image of OCAL-5; and (e–i) EDX element mapping of OCAL-5.

2.3. Characterization

The powder X-ray diffraction (XRD) patterns were recorded using Bruker AXS D8 Advance diffractometer operating with Cu-K α source to investigate the crystal structure of different samples. The morphologies of as-obtained samples were characterized by a field emission scanning electron microscopy (SEM; JEOL JSM 6700F, Japan) and transmission electron microscopy (TEM; JEOL 2010 HR & UHR). For SEM, the sample was dispersed on the surface of a copper sheet and coated with traces of platinum to enhance conductivity. Surface electronic state was analyzed by X-ray photoelectron spectroscopy (XPS; Thermo Fisher Scientific, UK). Specific surface area was characterized from nitrogen absorption-desorption data and Brunauer–Emmett–Teller (BET) measurement (ASAP2020, Micromeritics, USA). UV–visible diffuse-reflectance spectra (UV-vis DRS) were recorded in the range of 200–800 nm with a UV-2250 spectrometer equipped with an integrating sphere. Photoluminescence (PL) spectroscopy was measured on Perkin-Elmer LS-55 spectrofluorimeter at room temperature. The time-resolved fluorescence decay spectrum was performed on an Edinburgh FLS980 spectrophotometer with the excitation wavelength of 340 nm. The total organic carbon (TOC) assays were carried out using a Shimadzu TOC-VCPh analyzer. The electron spin resonance (ESR) signals of radicals spin-trapped by spin-trapped reagent 5, 5-dimethyl-l-pyrroline N-oxide (DMPO) and 2,2,6,6-Tetramethylpiperidinoxy (TEMPO) were examined via a Bruker ER200-SRC spectrometer under visible light irradiation ($\lambda > 420$ nm). Photoelectrochemical characterization were carried out with a CHI 660C electrochemical station in a standard three electrode configuration. Zeta potential of materials was measured by Zeta-sizer Nano-ZS (Malvern, UK).

2.4. Photocatalytic experiment

Photocatalytic degradation of methyl orange (MO) was carried out in a 250 mL beaker containing 100 mL MO solution (20 mg L^{-1}) and 30 mg of photocatalyst. The solution was magnetically stirred in a darkroom for 60 min to attain adsorption–desorption equilibrium. The solution was then irradiated under visible light illumination ($\lambda > 420$ nm). A 300 W Xenon lamp (Beijing China Education Au-light Co. Ltd) with a 420 nm cutoff filter was used as the visible light source. At certain time intervals, 3 mL aliquots were sampled and centrifuged to remove the particles. The residual MO concentration was determined using a UV–vis spectrophotometer at the wavelength of 463 nm. Similar process had also been carried out to degrade the 10 mg L^{-1} colorless bisphenol A with the photocatalyst amount of 0.6 g L^{-1} .

2.5. Density functional theory calculations

All density functional theory (DFT) calculations were performed with the Vienna Ab Initio Simulation Package (VASP) [33], and used the Projected Augmented Wave (PAW) method to describe ion-electron interactions [34]. The exchange and correlation effects were described by the Perdew–Burke–Ernzerhof (PBE) function [35]. A cut-off energy of 500 eV was set for the expansion of the plane-wave basis set. The gamma k-points were set for calculating the electronic structures. The value of $U = 2.5 \text{ eV}$ was applied to Co in this study. Bulk CoAl-LDH was built with a space group of $p\bar{3}m1$ and lattice parameters of $\alpha = \beta = 90^\circ$, $\gamma = 120^\circ$. The supercell of bulk CoAl-LDH was set to be $2 \times 2 \times 1$ in respectively the a , b , and c -direction with the molar ratio of Co : Al = 3 : 1. One carbonate ion is placed into the interlayer gallery of bulk CoAl-LDH to keep the charge neutral. For the optimization of the hybrid, a 20 Å of vacuum was added between the periodically repeated

slabs to avoid inter-slab interaction.

3. Results and discussion

3.1. Morphology and structure of photocatalyst

The SEM images of pure OCN, CoAl-LDH and OCAL-5 are presented in Fig. 2. Clearly, the pure OCN (Fig. 2a) exhibited thin and wrinkled two-dimensional structures. Oxalic acid might react with part of the amino groups in the urea, and then the oxygen atoms are incorporated into heptazine units in the thermal polymerization processes including isocyanic acid, biuret, cyanuric acid and melamine [32,36]. The obtained CoAl-LDH crystal nanosheets (Fig. 2b) were of hexagonal shapes sized between 3.0–6.0 μm . After dispersing the OCN sheets into aqueous solution via ultrasonication (Fig. 1), the positively charged Co^{2+} and Al^{3+} ion would be adsorbed on the surface of negatively charged OCN sheets with a zeta potential of -22.5 mV via electrostatic attraction. Under the hydrothermal condition, OCN sheets acted as a substrate to induce *in situ* growth of CoAl-LDH nanosheets crystallites, giving rise to flower-like structures via self-assembly, as shown in Fig. 2c and d. A large amount of OCN nanosheets dispersed uniformly on the surface of the CoAl-LDH substrate. Energy dispersive X-ray (EDX) spectroscopy demonstrates the existence of Co, Al, C, N and O elements in OCAL-5 (Fig. S2). EDX element mapping analysis is shown in Fig. 2e–i, which indicate that Co, Al, O, C and N element were homogeneously distributed throughout the particles. Therefore, a strong coupling interaction between the two layered materials through electrostatic binding interaction is likely. TEM images confirm the microstructure of the 2D porous structure of pure OCN (Fig. 3a) and hexagonal CoAl-LDH sheets (Fig. 3b). As for the OCN/CoAl-LDH hybrids (Fig. 3c), it is obvious that the CoAl-LDH nanoplatelets with a thickness of $\sim 16\text{ nm}$ are uniformly covered by a large amount of OCN sheets. From the high-resolution TEM image (Fig. 3d), the lighter-shade stripes reflect that OCN

exhibited lamellar and layer morphology. When the OCN combined with the CoAl-LDH sheets, the lattice strips of the CoAl-LDH sheets become less distinct, suggesting that the OCN nanosheets integrate compactly on the surface of the CoAl-LDH sheets to construct a well-defined sheet-on-sheet (2D-2D) heterostructure. The lattice fringes corresponding to the interplanar distance of 0.354 nm are attributed to the (012) plane of the CoAl-LDH phase. Similar observations on the microcosmic structure in 2D-2D heterojunctions have been demonstrated by past studies too [37–40]. The presence of diffraction rings in the electron diffraction (SAED) pattern (Fig. S3) demonstrates that the OCAL-5 is polycrystalline. The crystallinity of the OCAL-5 hybrids has been found to be dominated by hydrothermal processing time, as discussed in Fig. 4c.

Fig. 4 shows the PXRD patterns of pure OCN, pure CoAl-LDH and the corresponding hybrids. For pure OCN, there is a strong peak at 27.2° indexed as (002), which was ascribed to the interlayer stacking of aromatic systems [32]. The CoAl-LDH patterns exhibited a series of reflections at 2θ values of 11.7° , 23.5° , 34.6° , 39.1° , 46.8° , 60.3° and 61.6° , corresponding respectively to the (003), (006), (009), (012), (018), (110) and (113) lattice planes of a stacked LDH phase with CO_3^{2-} in the interlayer region [14,41]. In the case of the OCAL hybrids, Fig. 4a indicates a similar PXRD pattern of LDH, demonstrating the integration of these two semiconductors with high purity and degree of crystallinity. The diffraction peak of OCN at 18.6° , corresponding to the s-triazine based in-planar structural packing [42]. Moreover, Fig. 4b shows that the (003) diffraction peak of CoAl-LDH shifts from 11.7° to 11.5° , implying strong interaction between OCN and CoAl-LDH. After the diffusion and immobilization of the Co^{2+} and Al^{3+} ions through OCN via the electrostatic driving force, CoAl-LDH would be crystallized and formed. The crystal formation process of CoAl-LDH onto OCN has been investigated by time-dependent growth experiments. From the change in the PXRD patterns with time (Fig. 4c), the relatively poor diffraction peaks indicate the poor crystallinity of the hybrids at 6 h and

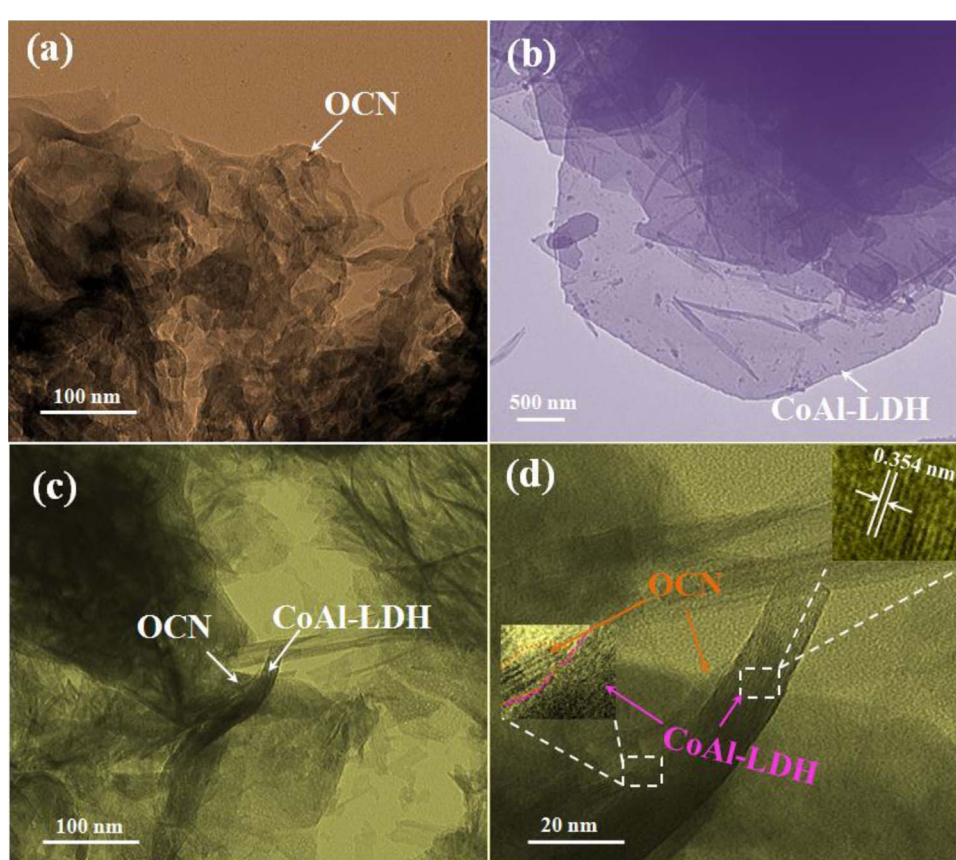


Fig. 3. TEM images of (a) pure OCN, (b) pure CoAl-LDH, (c) OCAL-5; and (d) high-resolution image of OCAL-5.

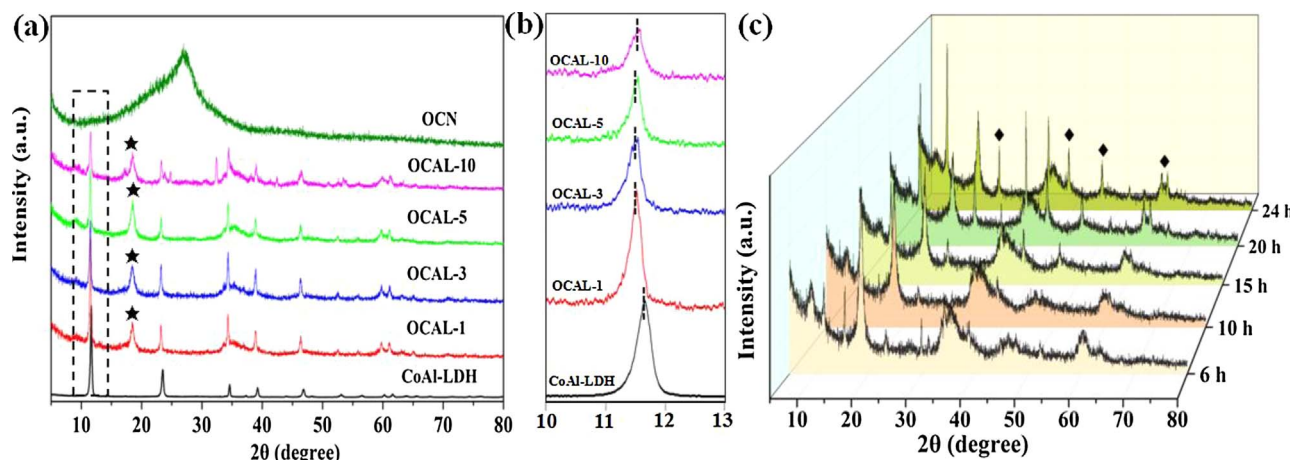


Fig. 4. (a) XRD patterns of OCN, CoAl-LDH and the corresponding hybrids; (b) magnified view of the main peak at around 11.6°; and (c) XRD patterns of OCAL-5 as a function of reaction time.

10 h, while several reflections like 60.3° and 61.6°, corresponding to LDH phase, apparently appeared at 15 h. More importantly, the intensities of the three peaks at 23.5°, 39.1° and 46.8° increased significantly upon prolonging the growth time to 24 h, further indicating the gradual crystallization and growth of high-quality hybrids. Collectively, it is inferred that the OCN/CoAl-LDH composites have successfully prepared, and the interfacial heterojunction structure may provide the bridging platform for photo-induced charge carrier transfer between the two semiconductors.

The surface area and porosity of photocatalysts play an important role in the photocatalytic performance. As shown in the N_2 adsorption/desorption isotherms (Fig. 5), typical IV type hysteresis loops (P/P_0), demonstrating the presence of mesoporous structures [43]. The average pore diameters of CoAl-LDH and OCAL-5 were respectively 26.8 nm and 12.1 nm, while the total pore volumes were respectively $0.15 \text{ cm}^3 \text{ g}^{-1}$ and $0.27 \text{ cm}^3 \text{ g}^{-1}$. Specifically, the OCAL-5 possesses a specific surface area of $89.3 \text{ m}^2 \text{ g}^{-1}$, which is much larger than that of the CoAl-LDH ($22.4 \text{ m}^2 \text{ g}^{-1}$). Moreover, the specific surface areas of OCAL-1, OCAL-3 and OCAL-10 were $43.7 \text{ m}^2 \text{ g}^{-1}$, $44.6 \text{ m}^2 \text{ g}^{-1}$ and $51.52 \text{ m}^2 \text{ g}^{-1}$, respectively. The relatively higher surface area, mesoporous feature and large pore volume may facilitate the exposure of the active sites during photocatalysis, and the diffusion of pollutant and active radical, thereby promoting the photocatalytic efficiency.

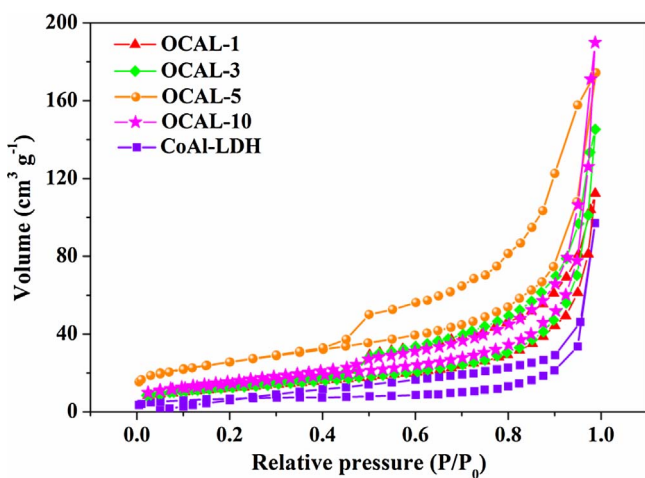


Fig. 5. N_2 adsorption-desorption isotherms of CoAl-LDH and OCAL-5.

3.2. Coupling interaction

Fine-scan X-ray photoelectron spectroscopy (XPS) is a rigorous tool to provide a better understanding of the interaction between OCN and CoAl-LDH. After exciting by the X-ray irradiation, the electron migration between two semiconductors can give rise to the binding energy shift for a specific element [44]. For the C 1s spectra of the OCAL-5 sample (Fig. S4), the peaks at 284.4, 286.3 and 288.8 eV can be ascribed respectively to the graphitic carbon, the C atom bonded with O (C–O) and sp^2 -bonded carbon (N=C–N) [32]. From Fig. 6a, the binding energies at 780.3 eV and 796.7 eV correspond to Co $2p_{3/2}$ and Co $2p_{1/2}$, respectively [45]. The appearance of satellite peaks implies the presence of a high-spin divalent state of Co^{2+} . For the OCAL-5, however, the binding energies of Co $2p_{3/2}$ and Co $2p_{1/2}$ shifted to 780.7 eV and 796.9 eV, respectively. Similar shifts are also evident in the XPS spectra of Al 2p (Fig. 6). The shifts of binder energy provide proof that the addition of OCN affected the electronic energy distribution of CoAl-LDH via the coupling interaction (or covalent bonding). Furthermore, the high-resolution XPS spectra of N1s and O1s have been analyzed. As shown in Fig. 6c, the N 1s spectrum of OCN sample displays four peaks centered at 397.7, 399.0, 400.1 and 404.0 eV, corresponding respectively to C=N=C, tertiary N atom (C₃–N) and amino functional groups (C₂–N–H) [32,46,47]. For the OCAL-5 hybrid, the N 1s peaks located at 399.0 eV and 400.1 eV shifted respectively by 0.9 eV and 0.5 eV towards the lower binding energy compared with that in OCN. This indicates that, for the tertiary nitrogen groups and amino functional groups, the lone pair electrons of sp^3 -hybridized N atoms as electron donors can interact with the unoccupied d orbitals of Co atoms or Al atoms to form Co–N bond or Al–N bond with the minimal space constraints. Such chemical coupling led to increased electron density in N atoms along with decreased electron density in Co or Al atoms to form covalent $\text{Co}(\delta^+)-\text{N}(\delta^-)$ or $\text{Al}(\delta^+)-\text{N}(\delta^-)$ bonding states [47,48]. From Fig. 6d, the O 1s peak of OCN at 531.2 eV was the C–O–C species, and the peaks at 530.9 eV and 531.9 eV correspond respectively to the Co–O and Al–O species in CoAl-LDH. Compared to pure OCN and pure CoAl-LDH, the negative shift to lower binding energy has occurred for the hybrids. Therefore, the XPS analysis simultaneously demonstrates the formation of the OCN/CoAl-LDH heterostructure at the atomistic level and the interfacial coupling interaction between the two semiconductors. It is expected to improve the photochemical properties like the separation and transfer of photo-generated charge carriers.

3.3. Optical and photoelectrochemical property

The photochemical properties are pivotal to the performance of

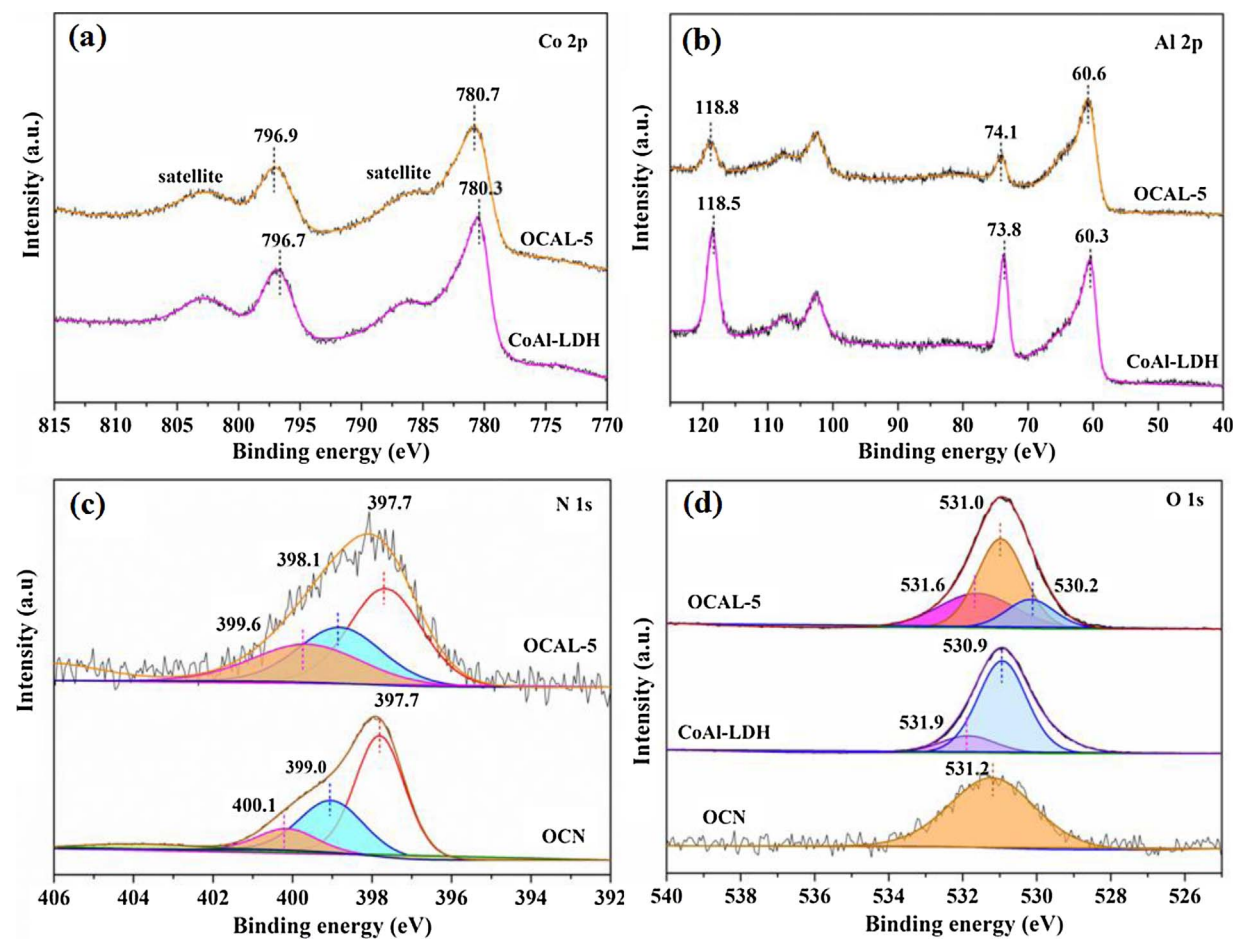


Fig. 6. High-resolution XPS spectra: (a) Co 2p, (b) Al 2p, (c) N 1s and (d) O 1s.

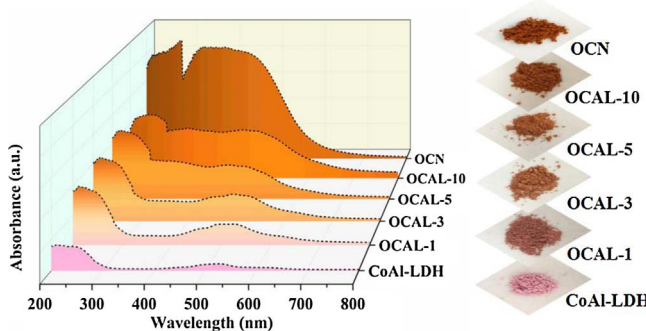


Fig. 7. UV-vis DRS of the as-obtained samples and the corresponding digital images.

photocatalysts. In this regard, solid diffuse reflection of UV-vis spectrum (UV-Vis DRS) was used to investigate the light response property of the photocatalysts synthesized. As illustrated in Fig. 7, pure OCN exhibited strong absorption from the ultraviolet to visible light range, and its band gap absorption edge was around 590 nm, whereas pure CoAl-LDH displayed relatively low absorption peak in the visible spectrum area. The band gaps of pure OCN and CoAl-LDH were approximately 2.09 eV and 2.1 eV, respectively, according to the Tauc plot in Fig. S5. As for the OCAL hybrids, a notable absorption extension in the visible-light range (400 ~ 800 nm) relative to the pure CoAl-LDH can be observed. Additionally, as the content of OCN in the hybrids increased, the optical absorption intensity was enhanced. The change of optical absorption properties is in accordance with the colour change of the photocatalysts. The observed strong absorption of visible light, relative to CoAl-LDH, suggests that these hybrids can be applied for

visible-light photocatalysis [12].

Photoluminescence and photoelectrochemical technologies can be considered as effective tools to understand the properties of photo-generated charge carrier capture, transfer and migration in photocatalysts. The photoluminescence (PL) spectra of pure constituents and resultant hybrids are shown in Fig. 8a (the inset image). The emission peak of OCAL-5 at 670 nm is lower than that of pure OCN and pure CoAl-LDH, implying the recombination of photo-excited charge carriers was highly suppressed because of the interfacial charge transfer between OCN and CoAl-LDH [25,49–51]. This process has been demonstrated by time-resolved transient PL experiments (Fig. 8a). The charge carrier lifetime of OCAL-5 was 2.21 ns, which was longer than that of pure OCN (1.96 ns) and pure CoAl-LDH (0.49 ns), reflecting the accelerated charge transfer induced by the heterojunction structure. In order to characterize the photo-induced charge migration, the photocurrent transient responses have been carried out under visible light and darkness in 0.5 mol L⁻¹ Na₂SO₄ aqueous solution (Fig. 8b). The photocurrent of the OCAL-5 electrode was much higher than that of pure OCN and pure CoAl-LDH, confirming the improved photoelectrical property and the separation efficiency of photo-generated electron-hole pairs. Furthermore, electrochemical impedance spectroscopy (EIS) Nyquist plots (Fig. S6) indicate that the OCAL-5 sample has the smallest arc radius compared to that of pure OCN, pure CoAl-LDH, and physical mixture of pure OCN and CoAl-LDH. It suggests that the OCAL-5 sample has the smallest electron-transfer resistance and highest electrical conductivity. The EIS results further demonstrate the formation of a heterojunction between pure OCN and CoAl-LDH, which expedite the transfer of photo-generated charge carriers. Moreover, this also indirectly implies that the faster electron transfer dynamics originates from the electric field in the interfacial heterojunction. Therefore, it is

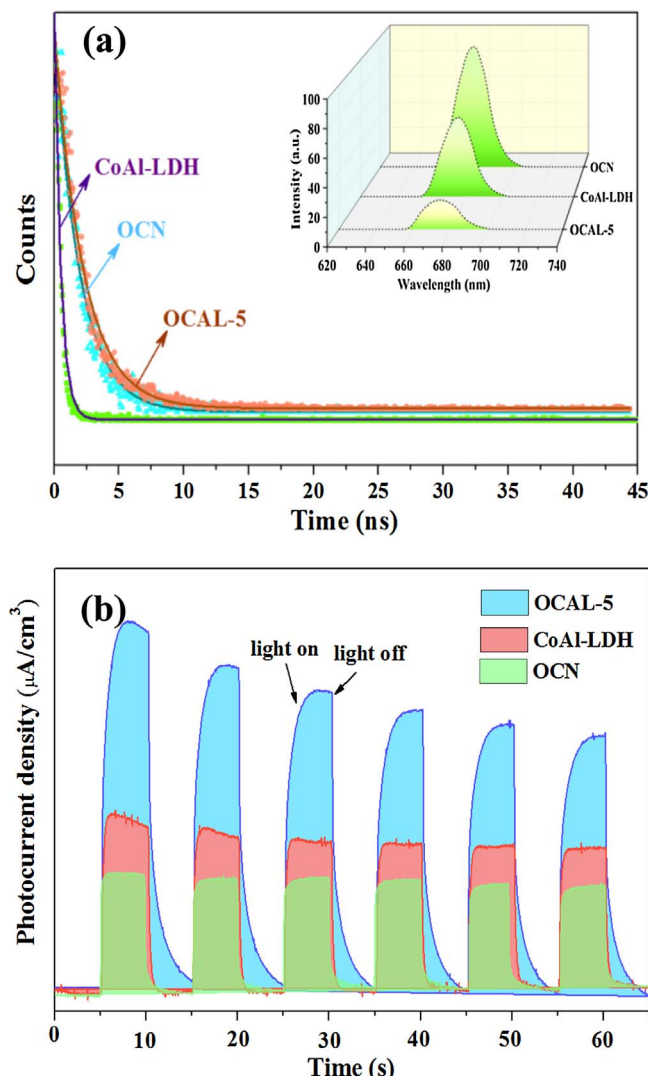
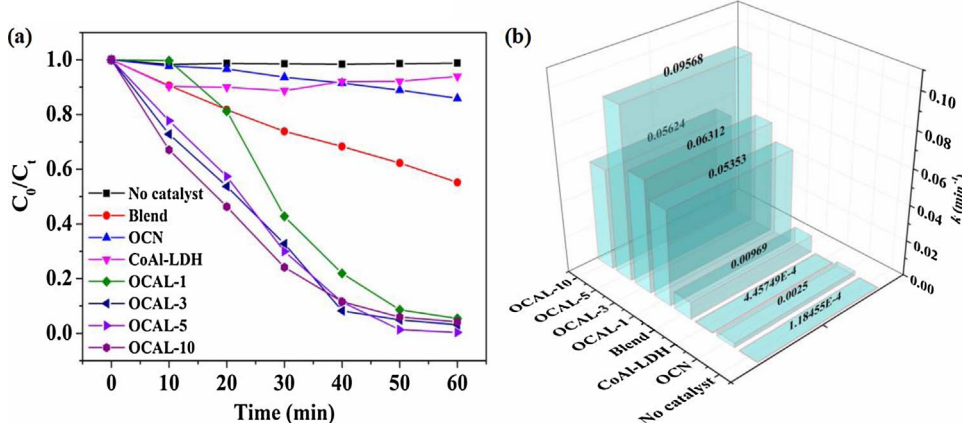


Fig. 8. (a) Time-resolved PL spectra of CoAl-LDH, OCN and OCAL-5, with the inset being the PL spectra; (b) Photocurrent (PC) response analysis of CoAl-LDH, OCN and OCAL-5 under intermittent visible light irradiation ($\lambda > 420$ nm).

reasonably inferred that the boosted photochemical properties promote the photocatalytic performance.

3.4. The evaluation of photocatalytic performance

Heterogeneous photocatalysis technology has been widely applied



in widespread environmental remediation applications such as air and water purification. Stable pollutant in water has been adopted here for assessing the photocatalytic activity of the as-prepared photocatalysts [52]. Before the pollutant degradation experiments, it has been determined that the adsorption-desorption equilibrium was attained within 60 min. The methyl orange (MO) photodegradation via the as-prepared photocatalyst were evaluated under visible light irradiation ($\lambda > 420$ nm). As shown in Fig. 9a, the pure OCN and pure CoAl-LDH only degraded 14.2% and 6.1%, respectively, of MO within 60 min, whereas all the OCAL hybrids exhibited higher photocatalytic degradation efficiency. This indicates that the synergistic effect can effectively enhance the photocatalytic activity of pure OCN and CoAl-LDH through photoinduced interfacial charge transfer at the OCN/CoAl-LDH heterojunction. Specifically, the specific surface area of OCAL-5 ($89.3 \text{ m}^2 \text{ g}^{-1}$) is larger than that of CoAl-LDH ($22.4 \text{ m}^2 \text{ g}^{-1}$), but lower than that of mesoporous OCN ($159.1 \text{ m}^2 \text{ g}^{-1}$). This trend is contradictory to the photocatalytic degradation performances of the different photocatalysts, and thus the effect of specific surface area is not the predominant factor in the photocatalytic decomposition of MO. The OCAL-5 hybrid with a MO removal efficiency of 99.7% has the best-performing photocatalyst. Moreover, for the colorless bisphenol A (BPA) degradation, a removal efficiency of 51.4% could also be obtained within 95 min, giving a degradation rate of 0.00829 min^{-1} under visible light exposure (Fig. S7). After three repeated degradation experiments, the MO removal efficiency is sustained at 90% (Fig. 10a), indicating good stability and reusability. The morphology (Fig. 10(b–c)) and crystallinity (Fig. 10(d)) of OCAL-5 has also changed negligibly after the photocatalytic reactions, demonstrating the excellent stability.

The kinetic curves for MO photodegradation over the various photocatalysts have been modeled according to the pseudo-first order model ($\ln(C/C_0) = kt$) and the values of k (i.e., rate constant) are shown in Fig. 9b. Clearly, the MO degradation rate is the fastest for OCAL-5 (0.09568 min^{-1}), followed by OCAL-3 (0.06312 min^{-1}), OCAL-10 (0.05624 min^{-1}), OCAL-1 (0.05353 min^{-1}), blend (i.e., no reaction) of OCN/CoAl-LDH (0.00969 min^{-1} , which is much lower than that of the OCAL hybrids), OCN (0.0025 min^{-1}), and lastly CoAl-LDH (0.0004 min^{-1}). Specifically, the highest degradation rate of OCN/CoAl-LDH hybrids is 38 and 239 folds higher than that of pure OCN and pure CoAl-LDH, respectively. This indicates that, as the OCN content increases in the hybrid photocatalysts, the photocatalytic activity increased then decreased. Because of the increased Co^{2+} or Al^{3+} adsorbed as OCN increased, more exposed heterojunction sites for charge transfer were created, which improved photocatalytic performance on one hand, but the quality and quantity of effective heterointerfaces favorable for charge transfer decreased which reduced photocatalytic performance on the other hand. This trend is consistent with different specific surface area in OCAL composites. The photocatalytic

Fig. 9. (a) Photocatalytic degradation of MO with time; and (b) pseudo-first order rate constants of OCN, CoAl-LDH and their hybrids. As a benchmark, the extent of degradation in the absence of any photocatalyst is also shown. “Blend” represents the physically blended (i.e., no reaction) sample of OCN and CoAl-LDH at the OCN content of 18.0%.

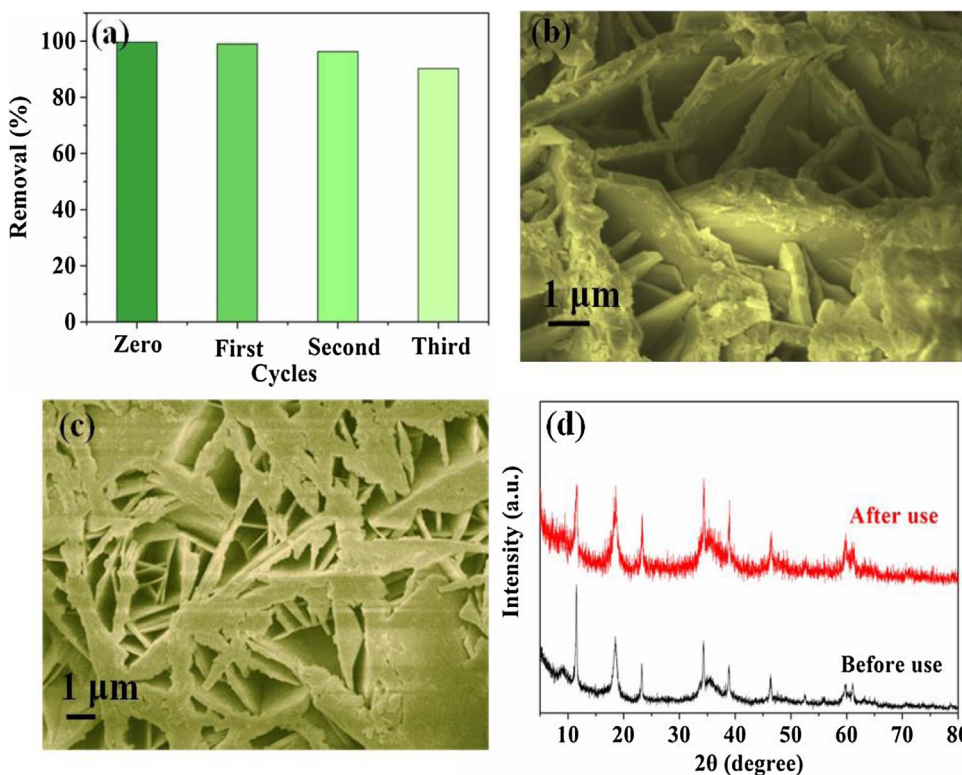


Fig. 10. Recyclability and stability tests of OCAL-5 for photodegradation of MO under visible light irradiation: (a) removal efficiency with repeated MO degradation; SEM images of OCAL-5 (b) before and (c) after four repeated MO degradation; and (d) XRD spectra of OCAL-5 before and after four repeated MO degradation.

performance of OCAL-5 as a function of reaction time during synthesis at the temperature of 110 °C is further shown in Fig. S8, which signifies that the photocatalytic activity improved as the synthesis reaction time increased. This indicates that the crystallinity and overall quality of the OCAL hybrids can be further optimized by adjusting the synthesis protocol.

3.5. Mechanism

To evaluate the photodegradation mechanism, the main oxidative species in the photocatalytic process have been detected through radical and hole trapping experiments using EDTA-2Na (h^+ scavenger), *p*-benzoquinone (O_2^- scavenger) and isopropyl alcohol ($\cdot OH$ scavengers). As shown in Fig. 11a, the photocatalytic degradation of MO is apparently restrained after the injection of EDTA-2Na, *p*-benzoquinone or isopropyl alcohol (IPA). The rate constant reduced from 0.09567 min⁻¹ in the photocatalytic system without any scavengers to 0.04554 min⁻¹, 0.00336 min⁻¹ and 0.0005 min⁻¹ in the presence of respectively IPA, *p*-benzoquinone and EDTA-2Na, which indicate that the MO degradation is most dependent on the oxidative species of holes (h^+) followed by O_2^- then lastly $\cdot OH$.

To further prove the existence of O_2^- and $\cdot OH$ in the photocatalytic system under visible light irradiation, the ESR spin-trap experiments have been performed on the OCAL-5 hybrid. All the experiments were operated in darkness and also visible light irradiation durations of 5 min and 10 min. As shown in Fig. 11b, the intensity of the DMPO- $\cdot OH$ adducts was negligible in the dark, but became greater with longer durations of visible light irradiation, demonstrating that the $\cdot OH$ played an important role in the photocatalytic process. Four characteristic peaks (Fig. 11c) of DMPO- $\cdot O_2^-$ in methanol dispersion under visible light irradiation appear, indicating that the $\cdot O_2^-$ was also produced. Furthermore, the holes (h^+) were also tested. As shown in Fig. 11d, the single-line signal ($g = 2.0025$) corresponds to the unpaired electron (or the delocalization of unpaired electrons) on the carbon atom of the aromatic rings within a π -bonded nano-sized cluster [53,54]. The intensities of the peaks increased when exposed to visible

light irradiation relative to that in the dark, demonstrating the existence of holes (h^+) and providing evidence of photo-induced carrier transfer between the OCN and CoAl-LDH. As a result, these reactive species could directly efficiently degrade the MO dye into other products. Total organic carbon (TOC) tests have been carried out to detect the amount of the carbon element in solution. During 60 min of visible irradiation, a mineralization rate of 40.3% TOC removal has been obtained, indicating that one part of MO was mainly mineralized to CO_2 and water, while the other part mainly decolorized.

To gain insights into the photocatalytic degradation mechanism in the OCAL photocatalyst, the separation processes of the photoexcited electron–holes can be described according to the band gap structures of OCN and CoAl-LDH, as shown in Fig. 12. According to previous reports, the conductor band and valence band of OCN (and CoAl-LDH) had been measured to 0.38 eV (−0.75 eV) and 2.46 eV (1.35 eV), respectively [19,32]. With regards to the charge carriers transfer of the OCAL photocatalyst, the electrons in the conductor band (CB) of CoAl-LDH will generally migrate to the CB of OCN, and holes in the valence band (VB) of OCN will migrate to the VB of CoAl-LDH, because the accumulated electrons in the CB of OCN ($E_{cb} = 0.38$ eV) cannot reduce O_2 to yield O_2^- ($E_{O_2/O_2^-} = -0.046$ eV), and the holes in the VB of CoAl-LDH cannot oxidize $\cdot OH$ to give $\cdot OH$. However, these oxidizing species have been clearly confirmed by the ESR signals for different samples (Fig. 11). Thus, the charge carrier transfer process of the OCAL heterojunction does not conform to the traditional Type-II model. According to the main oxidative species, it is reasonable to propose a Z-scheme charge transfer at the OCAL heterojunction under visible light irradiation (Fig. 12).

In order to understand the origin of photogenerated charge carriers transfer at the interfaces of the OCAL hybrid, DFT calculations have been carried out. According to the respective crystal structure (Fig. S9), the crystal models of the OCAL hybrid with the combinative interfaces composed of CoAl-LDH and OCN lattice planes had been constructed. Fig. 13a shows the OCAL crystal model after geometry optimization. The crystal structure indicates that the deformation degree of the OCN lattice at the interface is much larger than that of CoAl-LDH. This

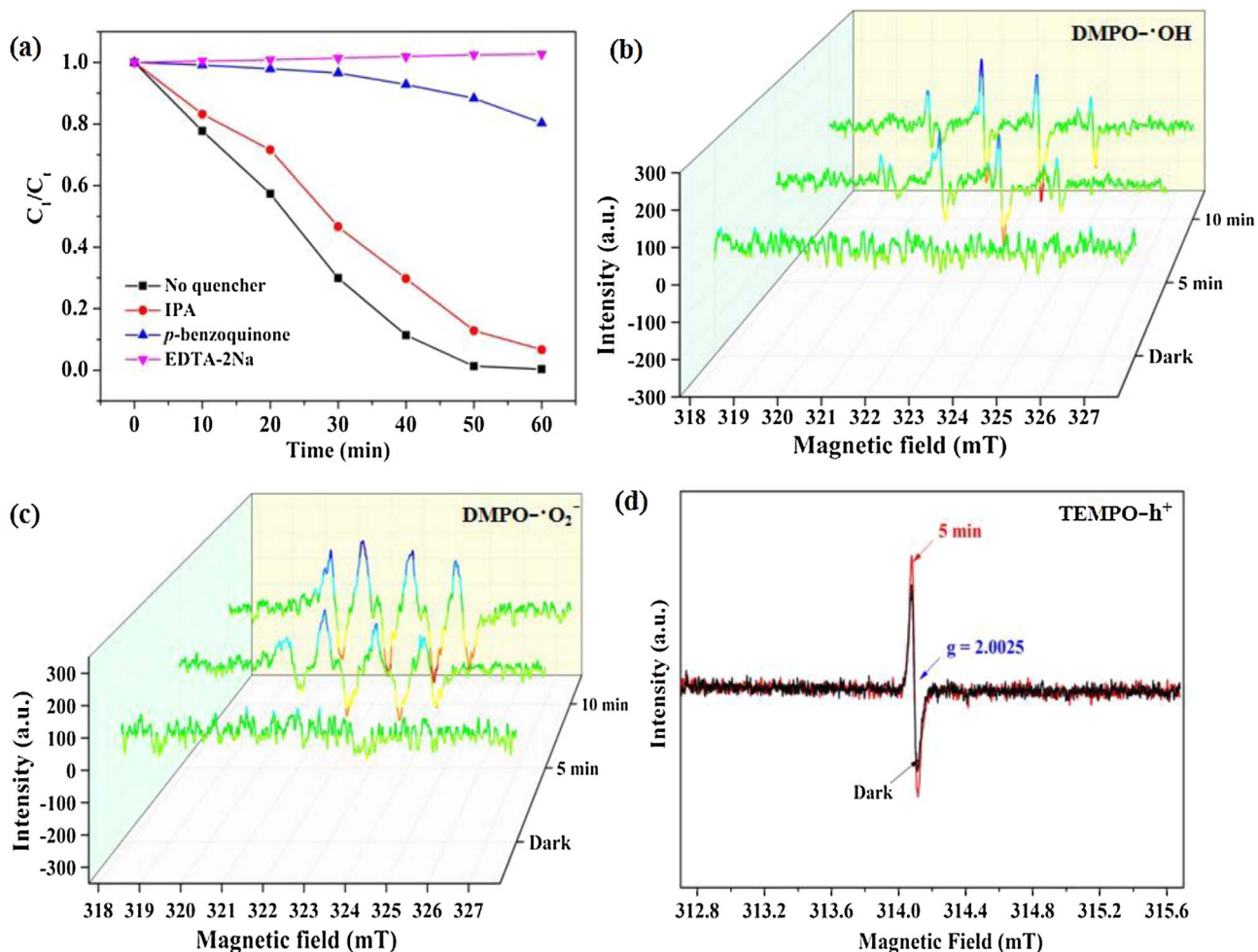


Fig. 11. (a) Effects of different reactive species scavengers on the photodegradation of MO by OCAL-5 under visible-light irradiation; ESR spectra of radical adducts trapped in the dark and under visible light irradiation by: (b) DMPO-OH in aqueous dispersion; (c) DMPO-O₂⁻ in methanol dispersion; and (d) TEMPO-h⁺ in aqueous dispersion.

conformational change does not only stabilize the Fermi level, but also enhances the depth of π -holes, which may affect the charge carriers transfer and catalytic performance at the interface [55]. The nearest distance between the N atom of OCN and the hydrogen atom at the CoAl-LDH surface is 1.68 Å, presumably suggesting the existence of pronounced hydrogen bonds at the interface. A similar phenomenon had been reported by Dou et al. [14]. Furthermore, the electron density difference (EDD) diagram is shown in Fig. 13b. Based on the Bader charge analysis [34], the direction of charge transfer is from CoAl-LDH to OCN, and the transfer amount is about 0.59 electrons at the interface, resulting in a decrease of charge concentration in CoAl-LDH and an increase in OCN. These results indicate the generation of interfacial internal electric fields (IEEF) between CoAl-LDH and OCN, with the transfer being from CoAl-LDH to OCN. As shown in Fig. S10, the flat potential (E_{fb}) of OCN and CoAl-LDH have been calculated to be respectively 0.18 and -0.95 V (vs. Ag/AgCl), which can be converted respectively to 0.38 eV and -0.75 eV (vs. NHE). The different flat potentials of OCN and CoAl-LDH indicates the existence of potential difference. After the combination by chemical interaction, the Fermi levels of OCN and CoAl-LDH can be adjusted and even flattened via the interfacial electron transfer between the two components [56,57]. The flattening of Fermi levels and subsequent electron flow could not only improve the band structure, but also create charge disequilibrium in the interfacial heterojunction, generating the built-in electric field between the layers with two different compositions. A similar phenomenon had been observed by Yu et al. [57]. The interfacial electric field makes the free charge carrier consume or accumulate near the semiconductor

surface compared with the bulk, ultimately causing the bending of energy band edges toward the interface [44,58]. This may switch photoinduced charge transfer from Type-II to Z-Scheme mechanism (Fig. S11) had also been demonstrated by Huang et al. [44]. This is to say, the downward band bending in one semiconductor permits the electrons flow out freely while prevents the holes flow out [59,60]. Meanwhile, the holes in the other semiconductor migrate along the upward band bending but the electrons do not. At last, the recombination of effusive electron and holes in individual semiconductor is the only way at the heterojunction interface.

As a result, the IIEF-induced direct Z-scheme charge transfer mechanism can be proposed to illustrate the radical generation as well as the enhanced photocatalytic activity (Fig. 12). Under visible light irradiation, both OCN and CoAl-LDH can be excited to produce electron-hole pairs. The electrons of OCN will recombine rapidly with the holes of CoAl-LDH via the direct solid-solid contact interface [9]. The photo-induced electrons in the CB of CoAl-LDH, which have more negative potential, reduce molecular oxygen to form abundant active O₂⁻, and the holes in the VB of OCN, which have more positive potential, generate ·OH radicals. A typical all-solid-state Z-scheme photocatalyst is favorable for the production of O₂⁻ and ·OH radicals, which is in agreement with the analysis of photocatalytic activity and reactive species of the OCAL photocatalyst. The intimate and large contact interfaces favor the effective charge transfer, leading to higher photocatalytic activity of the 2D-2D heterojunction. The formed strong oxidizing radicals could efficiently degrade MO into CO₂, H₂O and other by-products.

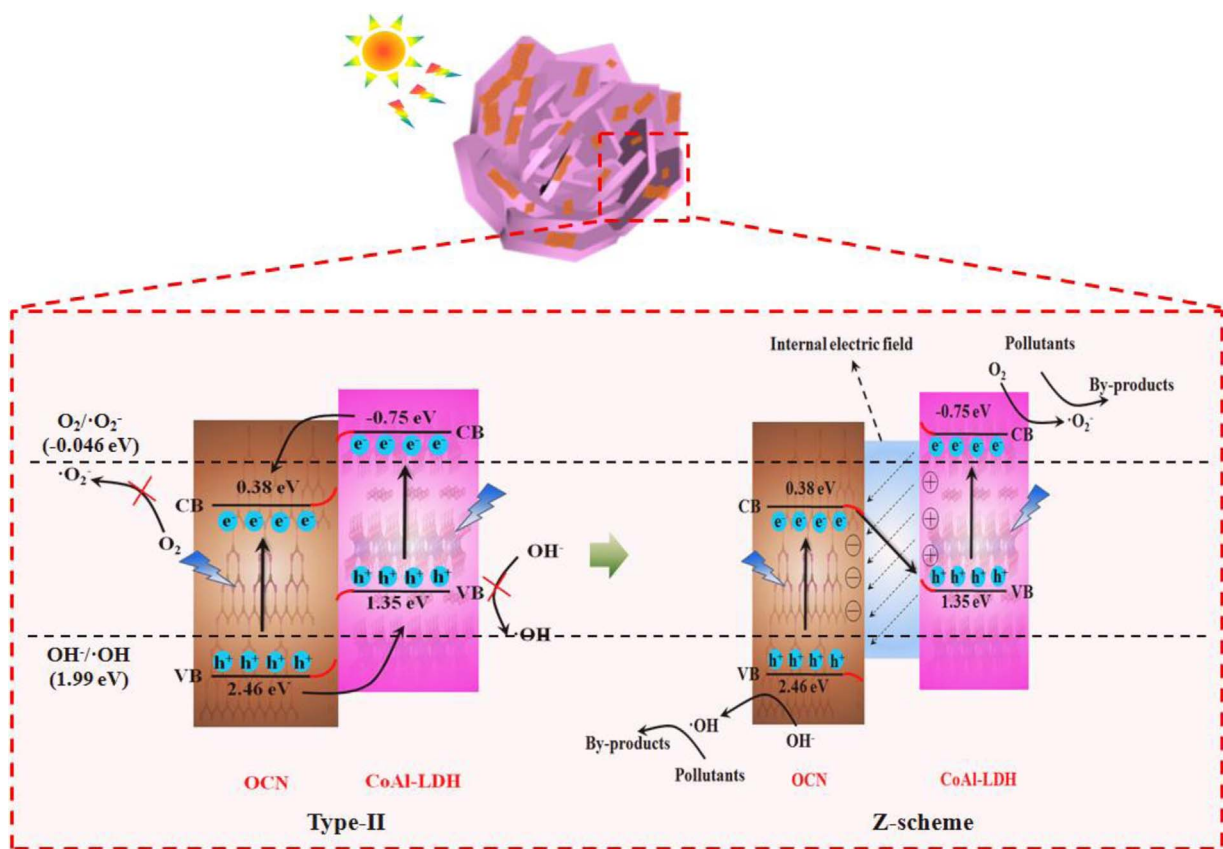


Fig. 12. Photocatalytic mechanism of OCAL-5 based on IIEF-induced direct Z-scheme charge transfer for pollutant degradation.

4. Conclusion

A 2D-2D heterostructure consisting of oxygen-doped carbon nitride (OCN) and ultrathin CoAl-layered double hydroxide (CoAl-LDH) with

the aid of hydrogen bonding had been constructed via the *in situ* growth method. The novel type of photocatalyst had relatively high surface area, mesoporous heterostructure, visible-light absorption property and excellent photogenerated charge carrier separation capability.

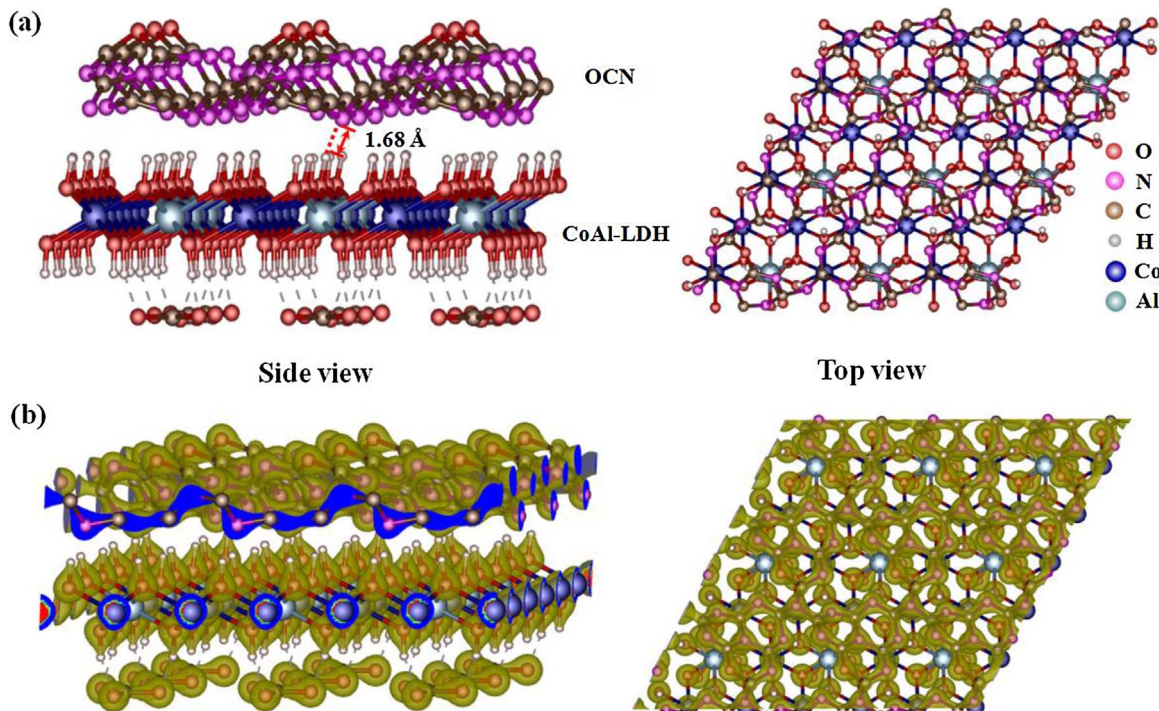


Fig. 13. (a) Crystal models after geometry optimization; and (b) calculated electron density difference (EDD) diagram (note that the blue area represents increase of electron density).

Specifically, the as-obtained photocatalyst with an OCN content of 18.0 wt% showed excellent visible-light photocatalytic degradation efficiency towards pollutant removal in water with a degradation rate of 0.09568 min^{-1} , which was 38 and 239 folds higher than that of pure OCN and pure CoAl-LDH, respectively. The improved photocatalytic performance was ascribed to the strong electronic coupling in the hybridized heterostructure interface, which could induce charge transfer from CoAl-LDH to OCN, resulting in the formation of an interfacial internal electric field (IIEF) between CoAl-LDH and OCN at equilibrium. An IIEF-induced direct Z-scheme charge transfer mechanism carried out under visible-light-driven excitation, with the recombination between the electrons of OCN and the holes of CoAl-LDH enhancing the extraction and utilization of photoinduced electron (or hole) in CoAl-LDH (or OCN), further facilitates the strongly oxidizing radical generation and thereby enhances photocatalytic degradation performance. The results of this work, which presents a kind of 2D–2D heterostructured platform for photocatalyst development and uncovers the nature of photo-induced charge transfer system in a novel hybrid photocatalyst, can be potentially employed in the fields of environmental remediation. However, since the dimension of each single component can be readily tuned by differing reactive conditions or template methods, more low-dimensional heterostructure systems (0D-1D, 0D-2D and 1D-2D) with outstanding photocatalytic activity will be expected for wide-ranging applications.

Acknowledgements

The authors gratefully acknowledge the financial support provided by the Singapore Ministry of Education Academic Research Funds Tier 2 (MOE2014-T2-2-074; ARC16/15) and Tier 1 (2015-T1-001-023; RG7/15), the GSK (GlaxoSmithKline) – EDB (Economic Development Board) Trust Fund, and the Joint Singapore-Germany Research Project Fund (SGP-PROG3-019). We also acknowledge funding from the Foundation for Innovative Research Groups of the National Natural Science Foundation of China (No. 51521006), the Key Project of National Nature Science Foundation of China (No. 51739004), and the Projects of the National Nature Science Foundation of China (No. 21776066, 51708195).

Appendix A. Supplementary data

Supplementary material related to this article can be found, in the online version, at doi:<https://doi.org/10.1016/j.apcatb.2018.01.069>.

References

- [1] C. Gao, J. Wang, H. Xu, Y. Xiong, *Chem. Soc. Rev.* 46 (2017) 2799–2823.
- [2] J. Low, J. Yu, M. Jaroniec, S. Wageh, A.A. Al-Ghamdi, *Adv. Mater.* 29 (2017) 1601694.
- [3] J.-P. Goddard, C. Ollivier, L. Fensterbank, *Acc. Chem. Res.* 49 (2016) 1924–1936.
- [4] G.J. Choi, Q.L. Zhu, D.C. Miller, C.J. Gu, R.R. Knowles, *Nature* 539 (2016) 268–271.
- [5] L. Jiang, X. Yuan, Y. Pan, J. Liang, G. Zeng, Z. Wu, H. Wang, *Appl. Catal. B: Environ.* 217 (2017) 388–406.
- [6] J. Liu, Y. Liu, N. Liu, Y. Han, X. Zhang, H. Huang, Y. Lifshitz, S.-T. Lee, J. Zhong, Z. Kang, *Science* 347 (2015) 970–974.
- [7] Z. Wu, X. Yuan, H. Wang, Z. Wu, L. Jiang, H. Wang, L. Zhang, Z. Xiao, X. Chen, G. Zeng, *Appl. Catal. B: Environ.* 202 (2017) 104–111.
- [8] X.-Y. Liu, H. Chen, R. Wang, Y. Shang, Q. Zhang, W. Li, G. Zhang, J. Su, C.T. Dinh, F.P.G. de Arquer, J. Li, J. Jiang, Q. Mi, R. Si, X. Li, Y. Sun, Y.-T. Long, H. Tian, E.H. Sargent, Z. Ning, *Adv. Mater.* 29 (2017) 1605646.
- [9] P. Zhou, J. Yu, M. Jaroniec, *Adv. Mater.* 26 (2014) 4920–4935.
- [10] C. Tan, X. Cao, X.-J. Wu, Q. He, J. Yang, X. Zhang, J. Chen, W. Zhao, S. Han, G.-H. Nam, M. Sindoro, H. Zhang, *Chem. Rev.* 117 (2017) 6225–6331.
- [11] H. Wang, X. Yuan, G. Zeng, Y. Wu, Y. Liu, Q. Jiang, S. Gu, *Adv. Colloid Interface Sci.* 221 (2015) 41–59.
- [12] H. Wang, X. Yuan, Y. Wu, G. Zeng, X. Chen, L. Leng, H. Li, *Appl. Catal. B: Environ.* 174–175 (2015) 445–454.
- [13] H. Wang, X. Yuan, Y. Wu, H. Huang, X. Peng, G. Zeng, H. Zhong, J. Liang, M. Ren, *Adv. Colloid Interface Sci.* 195–196 (2013) 19–40.
- [14] Y. Dou, S. Zhang, T. Pan, S. Xu, A. Zhou, M. Pu, H. Yan, J. Han, M. Wei, D.G. Evans, X. Duan, *Adv. Funct. Mater.* 25 (2015) 2243–2249.
- [15] H. Yin, Z. Tang, *Chem. Soc. Rev.* 45 (2016) 4873–4891.
- [16] Z.Z. Yang, F.H. Wang, C. Zhang, G.M. Zeng, X.F. Tan, Z.G. Yu, Y. Zhong, H. Wang, F. Cui, *RSC Adv.* 6 (2016) 79415–79436.
- [17] Y. Zhao, G. Chen, T. Bian, C. Zhou, G.I.N. Waterhouse, L.-Z. Wu, C.-H. Tung, L.J. Smith, D. O'Hare, T. Zhang, *Adv. Mater.* 27 (2015) 7824–7831.
- [18] H. Li, T.-N. Tran, B.-J. Lee, C. Zhang, J.-D. Park, T.-H. Kang, J.-S. Yu, *ACS Appl. Mater. Interfaces* 9 (2017) 20294–20298.
- [19] S. Kumar, M.A. Isaacs, R. Trofimovaite, L. Durnell, C.M.A. Parlett, R.E. Douthwaite, B. Coulson, M.C.R. Cockett, K. Wilson, A.F. Lee, *Appl. Catal. B: Environ.* 209 (2017) 394–404.
- [20] S. Kumar, M.A. Isaacs, R. Trofimovaite, L. Durnell, C.M.A. Parlett, R.E. Douthwaite, B. Coulson, M.C.R. Cockett, K. Wilson, A.F. Lee, *Appl. Catal. B: Environ.* 209 (2017) 394–404.
- [21] D. Deng, K.S. Novoselov, Q. Fu, N. Zheng, Z. Tian, X. Bao, *Nat. Nano* 11 (2016) 218–230.
- [22] K.S. Novoselov, A. Mishchenko, A. Carvalho, A.H. Castro Neto, *Science* 353 (2016).
- [23] X. Zhang, Z. Meng, D. Rao, Y. Wang, Q. Shi, Y. Liu, H. Wu, K. Deng, H. Liu, R. Lu, *Energy Environ. Sci.* 9 (2016) 841–849.
- [24] H. Wang, X. Yuan, H. Wang, X. Chen, Z. Wu, L. Jiang, W. Xiong, Y. Zhang, G. Zeng, *RSC Adv.* 5 (2015) 95643–95648.
- [25] Y. Liu, X. Yuan, H. Wang, X. Chen, S. Gu, Q. Jiang, Z. Wu, L. Jiang, Y. Wu, G. Zeng, *Catal. Commun.* 70 (2015) 17–20.
- [26] L. Jiang, X. Yuan, G. Zeng, X. Chen, Z. Wu, J. Liang, J. Zhang, H. Wang, H. Wang, *ACS Sustain. Chem. Eng.* 5 (2017) 5831–5841.
- [27] J. Fu, B. Zhu, C. Jiang, B. Cheng, W. You, J. Yu, *Small* 13 (2017) 1603938.
- [28] L.J. Fang, X.L. Wang, J.J. Zhao, Y.H. Li, Y.L. Wang, X.L. Du, Z.F. He, H.D. Zeng, H.G. Yang, *Chem. Commun. (Camb.)* 52 (2016) 14408–14411.
- [29] J. Li, B. Shen, Z. Hong, B. Lin, B. Gao, Y. Chen, *Chem. Commun. (Camb.)* 48 (2012) 12017–12019.
- [30] K. Li, Z. Huang, X. Zeng, B. Huang, S. Gao, J. Lu, *ACS Appl. Mater. Interfaces* 9 (2017) 11577–11586.
- [31] Y. Bu, Z. Chen, *Electrochim. Acta* 144 (2014) 42–49.
- [32] P. Qiu, C. Xu, H. Chen, F. Jiang, X. Wang, R. Lu, X. Zhang, *Appl. Catal. B: Environ.* 206 (2017) 319–327.
- [33] G. Kresse, J. Furthmüller, *Phys. Rev. B* 54 (1996) 11169–11186.
- [34] P.E. Blöchl, *Phys. Rev. B* 50 (1994) 17953–17979.
- [35] J.P. Perdew, K. Burke, M. Ernzerhof, *Phys. Rev. Lett.* 77 (1996) 3865–3868.
- [36] Y. Wu, H. Wang, W. Tu, Y. Liu, Y.Z. Tan, X. Yuan, J.W. Chew, J. Hazard. Mater. 347 (2018) 412–422.
- [37] D. Jiang, T. Wang, Q. Xu, D. Li, S. Meng, M. Chen, *Appl. Catal. B: Environ.* 201 (2017) 617–628.
- [38] J. Wang, L. Tang, G. Zeng, Y. Deng, Y. Liu, L. Wang, Y. Zhou, Z. Guo, J. Wang, C. Zhang, *Appl. Catal. B: Environ.* 209 (2017) 285–294.
- [39] X. Ma, D. Jiang, P. Xiao, Y. Jin, S. Meng, M. Chen, *Catal. Sci. Technol.* 7 (2017) 3481–3491.
- [40] H. Cheng, J. Hou, O. Takeda, X.-M. Guo, H. Zhu, J. Mater. Chem. A 3 (2015) 11006–11013.
- [41] H. Li, J. Li, C. Xu, P. Yang, D.H.L. Ng, P. Song, M. Zuo, *J. Alloys Compd.* 698 (2017) 852–862.
- [42] Y. Zhong, Z. Wang, J. Feng, S. Yan, H. Zhang, Z. Li, Z. Zou, *Appl. Surf. Sci.* 295 (2014) 253–259.
- [43] F. He, G. Chen, Y. Zhou, Y. Yu, Y. Zheng, S. Hao, *Chem. Commun.* 51 (2015) 16244–16246.
- [44] Z.-F. Huang, J. Song, X. Wang, L. Pan, K. Li, X. Zhang, L. Wang, J.-J. Zou, *Nano Energy* 40 (2017) 308–316.
- [45] G. Jia, Y. Hu, Q. Qian, Y. Yao, S. Zhang, Z. Li, Z. Zou, *ACS Appl. Mater. Interfaces* 8 (2016) 14527–14534.
- [46] J.-C. Wang, H.-C. Yao, Z.-Y. Fan, L. Zhang, J.-S. Wang, S.-Q. Zang, Z.-J. Li, *ACS Appl. Mater. Interfaces* 8 (2016) 3765–3775.
- [47] C. Li, Y. Du, D. Wang, S. Yin, W. Tu, Z. Chen, M. Kraft, G. Chen, R. Xu, *Adv. Funct. Mater.* 27 (2017) 1604328.
- [48] K.L. Corp, C.W. Schlenker, *J. Am. Chem. Soc.* 139 (2017) 7904–7912.
- [49] R.S. Varma, N. Thorat, R. Fernandes, D.C. Kothari, N. Patel, A. Miotello, *Catal. Sci. Technol.* 6 (2018) 8428–8440.
- [50] H. Wang, X. Yuan, H. Wang, X. Chen, Z. Wu, L. Jiang, W. Xiong, G. Zeng, *Appl. Catal. B: Environ.* 193 (2016) 36–46.
- [51] H. Wang, X. Yuan, Y. Wu, G. Zeng, W. Tu, C. Sheng, Y. Deng, F. Chen, J.W. Chew, *Appl. Catal. B: Environ.* 209 (2017) 543–553.
- [52] Z. Wu, X. Yuan, J. Zhang, H. Wang, L. Jiang, G. Zeng, *ChemCatChem* 9 (2017) 41–64.
- [53] Y. Li, S. Ouyang, H. Xu, X. Wang, Y. Bi, Y. Zhang, J. Ye, *J. Am. Chem. Soc.* 138 (2016) 13289–13297.
- [54] N.M. Dimitrijevic, S. Tepavcevic, Y. Liu, T. Rajh, S.C. Silver, D.M. Tiede, *J. Phys. Chem. C* 117 (2013) 15540–15544.
- [55] L.M. Azofra, D.R. MacFarlane, C. Sun, *Phys. Chem. Chem. Phys.* 18 (2016) 18507–18514.
- [56] R.A. Marcus, *J. Chem. Phys.* (1956) 966.
- [57] Y. Yu, W. Yan, X. Wang, P. Li, W. Gao, H. Zou, S. Wu, K. Ding, *Adv. Mater.* (2018) 1705060.
- [58] T. Di, B. Zhu, B. Cheng, J. Yu, J. Xu, *J. Catal.* 352 (2017) 532–541.
- [59] Y. Gao, J. Zhu, H. An, P. Yan, B. Huang, R. Chen, F. Fan, C. Li, *J. Phys. Chem. Lett.* 8 (2017) 1419–1423.
- [60] Z. Zhang, J.T. Yates, *Chem. Rev.* 112 (2012) 5520–5551.